

***In situ* observation of the deformation and fracture of an alumina-alumina ceramic-matrix composite at elevated temperature using x-ray computed tomography**

For submission to: Journal of the European Ceramic Society

Talha J. Pirzada^a, Dong Liu^{a,b,*}, Jon Ell^c, Harold Barnard^d, Ivo Šulák^e,
Marina Galano^a, Thomas J. Marrow^a and Robert O. Ritchie^{c,f}

^a *Department of Materials, University of Oxford, UK*

^b *School of Physics, University of Bristol, UK*

^c *Materials Sciences Division, Lawrence Berkeley National Laboratory, USA*

^d *Advanced Light Source, Lawrence Berkeley National Laboratory, USA*

^e *Institute of Physics of Materials, The Czech Academy of Sciences, Czech Republic*

^f *Department of Materials Science & Engineering, University of California, Berkeley, USA*

*Corresponding author: dong.liu@bristol.ac.uk

Abstract

The deformation and fracture of a 0/90° Nextel 720 alumina/Mullite fibre / alumina matrix ceramic-matrix composite material has been observed by *in situ* synchrotron x-ray computed micro-tomography at ambient temperature and at 1100°C. A three-point loading configuration was used and samples were loaded monotonically until final fracture. The flexural strength was found to be unaffected by temperature. 3D visualisation of the microstructure showed fracture occurred by propagation of internal cracks at stresses close to the flexural strength. Shear fractures propagated across fibre bundles that were oriented perpendicular to the flexural stress at both room temperature and 1100°C. At the higher temperature, an additional failure mode of delamination was observed, that may arise from relaxation of thermal residual stresses and creep.

Keywords: Ceramic-matrix composites; Oxide-oxide composite; X-ray computed micro-tomography; Digital volume correlation; *In situ* mechanical testing; failure mechanisms

1. Introduction

Oxide ceramic-matrix composites (CMCs) are used as structural materials in high temperature oxidising environments [1]. Due to their thermal stability, continuous fibre oxide-based CMCs have been used to make aircraft exhaust components *e.g.*, nozzle flaps [2,3], light weight helicopter exhaust ducts [2,4], sealing/casting shrouds and stationary vanes in gas turbines [3,5]. Compared with SiC CMCs, oxide CMCs offer a superior environmental stability and can be made into larger components at significant lower cost as processing does not involve repetitive reinfiltration or pyrolyzation steps [3,6]. For example, alumina (Nextel 720) fibre-based CMCs have been proposed for novel revolutionary combustors [7] that will shorten the combustion length by up to 50%. Furthermore, compared to the aerospace alloys currently being used for gas turbine seals, oxide CMCs can provide resistance to creep at temperatures 200-300°C higher than current operating temperatures [3].

CMCs can be considered to have three primary components: the fibre, the matrix and the fibre/matrix interface. The interface is often a weak boundary that plays an important role in improving the fracture toughness, since when a crack that typically originates in the matrix reaches the interface, delamination along that interface can deflect the crack. This increases the fracture resistance of the composite relative to its monolithic form [4]. However, if the interfacial layer is too strong, cracks can propagate into the fibre instead, causing a reduction in toughness [8]. In SiC fibre-SiC matrix composites, it is common to use boron nitride or carbon at the interface, but most oxide CMCs employ a weaker, more porous matrix as a substitute for an interface phase [7]. Three different matrices are currently available for high-temperature oxide CMCs [6]: alumina, mullite (the only chemically stable intermediate phase in the $\text{SiO}_2\text{-Al}_2\text{O}_3$ system) and aluminosilicate (compounds of aluminium, silicon and oxygen with substitution by other elements).

Due to the orthotropic nature of the material systems, the strength and stiffness depend on the load direction relative to the fibre directions. For example, the stress-strain behaviour of a Nextel 720/aluminosilicate sample, tested in bending, was found to be stable up to 1100°C with 0/90° ply orientation [9]. As the ply orientation was changed to $\pm 45^\circ$, significant anisotropy in the mechanical properties was observed. This was attributed to the generation of a tensile stress along the $\pm 45^\circ$ orientation relative to the weak fibre/matrix interface. There was also a difference of three to four orders of magnitude in the creep rate at 1100°C, from 10^{-9} s^{-1} in the 0/90° sample to 10^{-5} s^{-1} for the samples with $\pm 45^\circ$ orientations [7]. The strength of composites comprising aluminosilicate fibres within a mullite matrix [9] or alumina matrix generally remains unchanged after aging at 1200°C for 1000 hr, although significant weakening can occur in the aluminosilicate matrix system at temperatures of $\sim 1200^\circ\text{C}$. Electron microscopy investigations have shown that the aluminosilicate matrix begins to sinter at 1100°C, whereas the fibre (Nextel 720) microstructure remains unchanged [9].

The matrix properties can be optimised to improve high temperature performance; for instance, the introduction of a small amount of yttrium aluminium garnet significantly slowed the sintering of the alumina at 1300°C [10] and helped maintain its strength at elevated temperatures. Nano-particles may also be added to the matrix to modify its properties. For instance, with the additions of SiC nanoparticles the tensile creep rate of a mullite matrix composite was reduced to a much lower value of $2.9 \times 10^{-8} \text{ s}^{-1}$ at 1400°C, which is roughly four times less than that of the monolithic mullite [11]. Different oxide fibres can perform optimally under different conditions. In a study of the long-term tensile creep behaviour of oxide ceramic-matrix composites [12] tested at temperatures up to 1100°C, the materials with Nextel 610 fibres exhibited higher strength and stiffness, in contrast to another study [3], the materials with Nextel 720 fibres had lower strength and stiffness but performed better in

terms of creep at 1100°C. The creep resistance of Nextel 720 fibre/alumina matrix CMCs can degrade at temperatures higher than 1100°C in steam environments [13].

In situ observations of damage development within ceramic composites is essential in providing an in-depth understanding of the mechanical interactions between the matrix, fibres and porosity [14], as these cannot be accessed by surface observations. The application of high-resolution computed x-ray tomography (μ XCT) allows new insights into damage development within ceramic composite microstructures, and when such *in situ* studies are coupled with digital volume correlation (DVC) [15] it is possible to quantify the deformation and strain states [16,17] and their interactions with the architecture of the composite [16]. High temperature *in situ* observations are also feasible, as shown by a recent study involving real-time synchrotron x-ray tomography during uniaxial tension testing above 1600°C of a SiC-SiC composite [18] to investigate fracture propagation through the woven microstructure, including the influence of oxidation.

The objective of this work was to adopt this *in situ* approach to study failure in a Nextel 720 fibre / alumina matrix CMC at ambient temperature and at 1100°C, and document the evolution of damage with particular attention to the initiation of cracks and their subsequent propagation within the microstructure.

2. Experiments and Materials

The material under study was an oxide ceramic-matrix composite, fabricated by Composite Horizons, LLC (PPC structurals, USA) with an eight harness-satin weave in the 0/90° orientation. The matrix is alumina (Al_2O_3) and the Nextel 720 fibres (Al_2O_3 with 15% SiO_2 addition) have a diameter of 10-12 μm ; no interfacial layer was added between the fibre

1 and the matrix. The matrix was fabricated by slurry infiltration, by which a slurry containing
2 ceramic Al₂O₃ particles wicks into the porous fibre preform cloths [12] to form a matrix-
3 infiltrated prepreg. The cloths were then stacked and consolidated using vacuum bagging at a
4 temperature of around 150°C to drive out water or any remaining solvents. This was followed
5 by pressureless sintering in the range of 1000-1200°C. The surfaces of the CMC plate were
6 ground (Hauser S 35 400 CNC), with a tolerance of 0.1 mm, using a SiC cutting tool.

7 Prior to the in-situ experiments, the microstructure of a rectangular specimen (15 × 4 × 5
8 mm) was first examined with laboratory tomography using a Zeiss Xradia 510 Versa 3D x-
9 ray microscope, operating at 80 kV energy with 7 W power. The tomograph was
10 reconstructed from 2001 projections (10.9 s per projection) recorded over a 360° rotation,
11 with 2× binning of the 2048 × 2048 pixel camera, to visualise a cylindrical region of interest
12 (~2.7 mm diameter × 2.7 mm height) at a voxel size of 2.7 × 2.7 × 2.7 μm³. The specimen's
13 longest dimension was parallel to the rotation axis to minimise the x-ray path length. The
14 tomograph was reconstructed using the instrument software, and then visualised and post-
15 processed using the Avizo software (Version 9.5.0b).

16 *In situ* x-ray tomography experiments were conducted at beamline 8.3.2 on the Advanced
17 Light Source, at the U.S. Lawrence Berkeley National Laboratory [19]. During the
18 experiments, a unique device that permits mechanical loading at elevated temperatures was
19 used [20]; details of the device can be found in ref. [18]. Its central part is an aluminium
20 chamber (~150 mm in diameter) where the heating is provided by six ellipsoidal 150 W
21 Halogen lamps which illuminate a uniform hot zone region (~0.5 cm³). The test specimen
22 was positioned in the hot zone, and in line with a 300 μm thick aluminium window to allow
23 x-ray transmission from the source (white beam, 6 - 43 keV) to the detector. The field of

view on the detector (PCO Edge 2× CCD camera, 2560×2560 pixels) was 8×4 mm (voxel size: $3.25 \mu\text{m}$); for higher resolution characterisation, it was reduced to 3.2×2.6 mm (voxel size: $1.3 \mu\text{m}$). In each scan, 1969 projections were collected over a rotation of 180° , with an acquisition time of 30 ms for each projection (time per tomograph approximately 17 minutes). Rectangular beam specimens, with dimensions of approximately $2 \times 3 \times 20$ mm were tested at the lower resolution, and with dimensions of $1.75 \times 1.75 \times 20$ mm at the higher resolution. These were loaded using a three-point bending configuration with a 16 mm span (the diameter of the loading rollers was 3 mm).

Tests were conducted at two temperatures: RT (nominally 25°C) and 1100°C . Two samples were tested at each temperature, with one of these observed by tomography for RT at $3.25 \mu\text{m}$ voxel size. Two samples observed by tomography for 1100°C at two different voxel sizes: Sample S1 was imaged at $3.25 \mu\text{m}$ voxel size, and Sample S2 was imaged at $1.3 \mu\text{m}$ voxel size. A thermocouple was placed in contact with the side of the sample to control the temperature via the lamp current. For each *in situ* tomographed sample, several scans were undertaken from the pre-load (essentially load-free) condition until fracture. The reconstruction was performed using the Gridrec algorithm [21] with the centre of rotation of each scan individually identified. This was necessary to eliminate artefacts caused by deformation especially for the elongated vertically oriented samples under bending. Conventional flat field correction was used to normalise the acquired projection images to reduce the detector's fixed pattern noise. 3D visualisation and segmentation were undertaken subsequently using Avizo.

Digital volume correlation (DVC) of the synchrotron x-ray tomographs was carried out with the LaVision DaVis software (version 8.3.1) using the Direct Correlation procedure and

the pre-loaded tomograph as reference. The analysis of loaded tomographs from the room temperature experiment and the 1100°C sample S1 was carried out with a final subset size of $32 \times 32 \times 32$ voxels (*i.e.*, 32^3) at 75% overlap, using the pre-load tomograph as reference, after two passes each at successive cubic subset dimensions of 256^3 , 128^3 , 64^3 and 32^3 voxels. For the sample S2 tested at 1100°C, it was necessary to carry out the DVC analysis only to a larger subset size of 64^3 voxels at 75% overlap to reduce the noise that is inherent at smaller subset sizes. Post-processing of the three-dimensional displacement fields was performed using Matlab (Version 2017a).

Fractured samples were mounted in conductive epoxy resin and ground with 1200 grit SiC paper followed by successive 6 μm , 3 μm and 1 μm diamond paste polishing, prior to a final polish in colloidal silica (Col-K) with particle size of ~ 60 nm. The surface was then cleaned by a Gatan PIPS II ion polishing system for 2 hr at 6 kV beam voltage and an average beam current of 0.32 μA with an argon gas flow of $0.1 \text{ cm}^3 \text{ min}^{-1}$. Optical microscopy of the polished samples was undertaken using an Olympus GX51 Inverted Metallographic Microscope. A Nomarski contrast objective lens of 10 \times was used in bright field mode, with montage images obtained by image stitching using an ImageJ¹ plug-in². The samples were then coated with carbon, using a Q150R Plus plasma rotary pump sputter coater, to prevent charging before examination in a Carl Zeiss Merlin Field Emission Scanning Electron Microscope (Carl Zeiss SMT AG) at 5 kV with a probe current of 100 pA.

¹ Schneider, C.A., Rasband, W.S., Eliceiri, K.W. "NIH Image to ImageJ: 25 years of image analysis". *Nature Methods* 9, 671-675, 2012.

² ImageJ plugin: Preibisch S., Saalfeld S., Tomancak P. "Globally optimal stitching of tiled 3D microscopic image acquisitions", *Bioinformatics*, 25(11),1463-1465, 2009.

A Tescan Lyra3 XMU Focused Ion Beam Scanning Electron Microscope (FIB-SEM) was used to make thin foils for examination by transmission electron microscopy (TEM). A strip of platinum was deposited on the sample to protect the region of interest from material redeposition during FIB milling [22]. Trenches were cut to define the foil using a FIB voltage of 30 kV and a current of 4 nA, then at 30 kV/1 nA for surface cleaning. Each foil, with a width of $\sim 1\ \mu\text{m}$, was then cut free, transferred and mounted on a copper grid and then further thinned from both sides progressively to 300 nm at 30 kV/1 nA, to 100 nm at 30 kV/160 pA and then at 2 kV/20 pA to 50–60 nm thickness with the foil inclined at 2.5° from the optimal tilt angle. A JEOL 2100F STEM (200 kV) system with point-to-point resolution of 0.23 nm was used for observations in both bright field (BF) and annular dark field (DF-HAADF) STEM modes (2048×2048 pixels at $30\ \mu\text{s}$ per pixel). Diffraction images of fibres sectioned in both longitudinal and transverse directions from the room temperature sample were obtained using a camera length of 800 mm.

3. Results

3.1 Microstructure

The laboratory x-ray tomograph of an as-fabricated sample **Figure 1a** shows the fibre bundle orientations in the $0^\circ/90^\circ$ woven structure, where 0° fibres have been defined as being parallel to x axis and 90° fibres are parallel to the z axis. There are matrix cracks (either perpendicular to, or parallel to, the fibres) and porosity (mainly in the matrix and at the fibre bundle/matrix interface) (**Figure 1a, b**). The SEM images show the close packing of the fibres within the tows (**Figure 1c**), and fine pores (**Figure 1d**) in both the fibres and matrix. The total porosity of the tomographed sample (**Figure 1a**) was estimated to be around 24 vol.%, using volume thresholding in Avizo.

Imaging using transmission electron microscopy (TEM) (**Figure 2**) confirmed the porous interface between fibre and the matrix, with no difference distinguishable between the interface structures after testing at room temperature and at 1100°C. The TEM images of the fibre show an equiaxed structure with an average grain size of 50-100 nm. Diffraction patterns of the fibre shown in **Figure 3** are obtained from sections parallel (0°, 30°) and perpendicular (60°, 90°) to the fibre axis. The azimuthally integrated diffraction spectra in **Figure 3a** shows the peaks from cristobalite (SiO₂), mullite (Al₂O₃.SiO₂), and alumina (α -Al₂O₃) with the alumina phase dominant. The fibre has a preferred crystalline texture, shown (**Table 1**) by the change in relative integrated intensity of the {113} and {223} alumina peaks with observation angle relative to the fibre axis.

3.2 Fracture Behaviour

The load-crosshead displacement data acquired during the *in situ* synchrotron x-ray tomography tests at ambient and 1100°C provided nominal relationships for stress vs. strain, (**Figure 4**), which were obtained using the Euler–Bernoulli (slender beam, linear homogeneous elastic properties) analysis for small displacements. The flexural strengths at both RT and 1100°C were similar at approximately 100 MPa (**Table 2**). The flexural moduli were estimated from the linear region of the stress-strain curve (**Figure 4**); the low-load region was neglected as it shows the typical bedding-in characteristic of the mechanical testing of composites, whereas data at high stresses may be affected by damage from contact with the loading pins. The linear-elastic moduli obtained by this method at room temperature and 1100°C were ~50 GPa and ~40 GPa, respectively (**Table 2**).

In addition to a reference at the pre-load, tomographs were recorded close to ~80% and 100% of the peak loads. A tomograph was also collected for the RT sample at ~50% of the

1 peak load. These are respectively indicated as $0.5R\sigma$, $0.8R\sigma$ and $R\sigma$ in **Figure 4**. The regions
2 that were observed by tomography are identified in **Figure 5**; the loading pin is visible on the
3 top of the tomograph. A smaller region is indicated that contains the results of the digital
4 volume correlation (DVC) analysis. The nominal shear force and bending moment profiles
5 that the samples experienced during loading are also shown for reference, assuming Euler–
6 Bernoulli conditions.

7 A *post-mortem* analysis using optical microscopy (**Figure 6a**) shows that at RT, crack
8 propagation was inclined at an angle of approximately 45° to 60° with respect to the loading
9 axis, whereas the samples tested at elevated temperature showed complete delamination
10 (**Figure 6b**). Scanning electron microscopy confirmed the tendency for the crack to
11 propagate with local paths that were inclined to the loading direction, with crack deflection
12 also at the interfaces of 0° and 90° fibre tows (**Figure 6c**). At 1100°C , significant
13 delamination can also be seen; the sample also appears to be more friable as indicated by the
14 polishing damage in the circled regions in **Figure 6d**.

15 The room temperature *in situ* tomography data are summarised in **Figure 7a**, using
16 vertical sections (‘orthoslices’ in the y - x plane) across the central region of the sample with
17 the positions of the loading and support pins indicated. In region (i), which is beyond the
18 outer support pin and so outside the zone of maximum shear force, an initial vertically
19 oriented matrix crack was observed to close with increasing load. The formation of new
20 cracks was only observed above $0.8R\sigma$, within the zone of high shear force; examples are
21 identified in regions (ii) and (iii) and are presented at higher magnification in **Figure 7b**. The
22 cracks that were originally present in the matrix did not show any obvious extension. The
23 three-dimensional nature of cracks (ii) and (iii) is visualised in **Figure 8**, which shows crack
24 propagation along the interface between the $0/90^\circ$ fibre tows, with these inter-tow cracks

1 joined by sectors within the fibre tows at approximately 45° . These cracks extend across the
2 whole width of the sample.

3 Results are similarly presented in **Figure 9** for sample S1, which was tomographed at
4 1100°C with the same $3.25\ \mu\text{m}^3$ voxel size as the RT sample. **Figure 9** shows inclined cracks
5 at $\sim 45^\circ$, labelled (ii) and (iii), and interlayer cracks, labelled (i). The cracks are visualised in
6 three dimensions in **Figure 10**, which shows they also propagated across the whole width of
7 the cross-section, similarly to those observed at RT. The interlayer cracks (i) are needle-
8 shaped; such cracks were only observed at elevated temperature, mainly underneath the
9 loading pin (*i.e.*, at the maximum bending moment) in both tensile and compressive regions,
10 with some cracks also observed close to the support pin.

11 In Sample S2 (**Figure 11**) the region of maximum bending moment was tomographed at
12 1100°C at a voxel size of $1.3\ \mu\text{m}^3$. A typical pre-existing matrix crack is highlighted in region
13 (i). No new cracks are observed until $0.8R\sigma$ was exceeded. Examples of these new cracks are
14 indicated in regions (ii) and (iii); these interlayer cracks propagate along the interface
15 between the 0° and 90° fibre tows or parallel to the fibres within the tows. A 3D visualisation
16 of the cracks observed at $R\sigma$ is presented in **Figure 12**. As observed in sample S1 at 1100°C ,
17 they are needle-like in shape, with width between $15\text{--}20\ \mu\text{m}$, and are aligned with the x -
18 direction of applied load.

19 3.3 Analysis of Displacement Fields

20 DVC of tomographs provides three-dimensional displacement fields of the deformation
21 relative to the reference image. The results obtained at room temperature are presented in
22 **Figure 13a** as maps of the maximum normal 3D strain, calculated from the local gradients of

the displacement field (centred 3-point differentiation). Some quite localised strains are observed at low load ($0.5R\sigma$), but these strains are sensitive to errors in the low magnitude displacement field and may not be reliable. No significant strains are developed until $R\sigma$ is reached, and these strains are coincident with the newly developed cracks in regions (ii) and (iii) (**Figure 13b**). A more detailed analysis of the crack at region (ii) is presented in **Figure 14**, using the relative displacements between points separated by $\sim 100\text{ }\mu\text{m}$ across the crack; the values are averaged over 7 slices in the z -direction ($\sim 75\text{ }\mu\text{m}$). This finds significant opening and shear displacements of the crack; within the 45° inclined region (location D), the crack has an opening displacement of about $3.5\text{ }\mu\text{m}$, and a shear displacement of $\sim 6\text{ }\mu\text{m}$.

DVC analysis of sample S2 at 1100°C shows regions of high maximum 3D strain at $R\sigma$ (**Figure 15a**) that are coincident with newly initiated interlayer cracks such as those at regions (i) and (iii); these are presented in more detail in **Figure 15b**. There are no measurable strains associated with the vertical matrix cracks, which are present in the as-fabricated microstructure (ii), indicating that they do not open significantly. Analysis of the displacement field around a needle-shaped interlayer crack that developed within a fibre tow and along the fibre tow/matrix interface, following the same method as at ambient temperature (**Figure 16**), shows the crack shears by up to $\sim 10\text{ }\mu\text{m}$ and opens by up to $\sim 7\text{ }\mu\text{m}$. There is a smaller crack opening magnitude within the fibre tow than at the fibre/matrix interface.

The DVC-measured displacement fields allow the overall flexural behaviour of the specimens to be quantified. This was carried out by measuring the relative differences in x -displacement between points on two vertical (y - z) planes, positioned on either side of the central loading pin and separated by 0.7 mm (**Figure 17a**); within this region the bending moment is within 5% of its maximum value. The average strains, obtained from the

displacement change over the gauge length between the selected planes, are mapped in **Figure 17b**, for the RT data. The strains are approximately constant across the sample thickness (z -direction), indicating that bending of the specimen is well aligned, and there is a trend from compression to tension over the specimen height (y -direction). Measurements obtained for the DVC analysis at 1100°C are more noisy, but show the same trends; the data from all tests are summarised in **Figure 17c**, averaged across the specimen width and normalised by the ratio of bending moment (M) to second moment of area (I).

The effective elastic moduli of the beams were estimated from these strain data using the assumptions of simple Euler–Bernoulli bending. This assumes isotropic properties and neglects any movement of the neutral axis and fits a linear gradient to the variation of flexural strains, ϵ_x , with position y to calculate the beam’s radius of curvature, R :

$$M = EI/R \text{ and } \frac{d\epsilon_x}{dy} = -1/R, \quad (1)$$

where M is the change in the applied bending moment, I is the second moment of area of the beam and E is the elastic modulus [23]. The effective elastic moduli were calculated using a linear regression analysis of the normalised data, averaged across the specimen width (**Figure 17c**); the resulting values are summarised in **Table 3**. The room temperature modulus at 0.5R σ was ~38 GPa, but it was progressively reduced with increasing load at 0.8R σ and R σ . At 1100°C, the modulus for Sample S2 was approximately 40 GPa at 0.8R σ and reduced with increasing load at R σ . Sample S1 had a low modulus of around 27 GPa at R σ .

4. Discussion

The microstructure of the Nextel 720 fibre/alumina matrix ceramic matrix composite is similar to that reported by Tandon *et al.* [24]. The inherent matrix porosity and

defects(cracks, **Figure 1**) are caused by matrix shrinkage during processing [25,26]. The elastic moduli in **Table 2** were estimated using the cross-head displacement, and so are not necessarily accurate, but the relative magnitudes of the flexural strengths and moduli are consistent with similar biaxial oxide/oxide composites, albeit in the lower range [27]. A previous review [7] found no significant effect of temperature up to 1100°C on the strength and modulus for 0°/90° composites of Nextel 720 fibres in an alumina-silicate matrix for tensile loading parallel to the fibre bundles. This is consistent with the data in this study; the measured difference in strength with temperature (**Table 2**) for the small number of samples tested is not statistically significant. The initial porosity of these composites is high (>24 vol.%), due to matrix and interface cracks, but is similar to that observed in comparable oxide-oxide composites [28].

Analysis of the *in situ* x-ray tomographs using DVC to measure local displacements allows discrimination between new cracks and the inherent defects that formed during manufacture; the latter did not open or propagate measurably (**Figure 14** and **Figure 16**). Significant new cracks were observed to initiate and propagate only close to the maximum flexural strength, though the possible formation of fine cracks below the resolution of μ XCT cannot be discounted [29]. The effective elastic moduli, obtained by specimen curvature measurement via DVC (**Table 3**), do not measure the actual tensile Young Modulus, due to the gradient of strain in flexure and anisotropic properties of the composite. Nonetheless they are a measure of the flexural stiffness of the composite specimen. This shows that in the absence of visible new damage (*i.e.*, up to 0.5R σ at RT and up to 0.8R σ at 1100°C), the moduli are similar at RT and 1100°C. The reduction in effective modulus observed at higher loads can be attributed to the development of damage, which acts to reduce the composite stiffness.

1 The TEM observations (**Figure 2**) show no difference between the structure of the
2 interfaces of samples tested at room temperature and at 1100°C. However, the increase in
3 temperature to 1100°C has significantly changed the failure patterns; at room temperature,
4 the fracture was inclined across the fibre bundles (**Figures 7, 8**), whereas at 1100°C the
5 fracture propagated similarly to room temperature, but also between the fibre bundles leading
6 to complete delamination.

7 At both room temperature and 1100°C, cracks initiated in regions of high shear and low
8 bending moment (**Figure 13**), and consequently the crack openings displayed a significant
9 shear displacement (**Figure 14**). The inclined crack path through the 0° fibre bundle, in
10 which the fibres are oriented in the z -direction and loaded orthogonally in the x -direction,
11 implies the fibre interfaces within the fibre bundle have low strength. A significant crack at
12 room temperature (**Figure 13**, region (ii)), which also generated inclined fracture across the
13 0° fibre bundle, developed in the region below the neutral axis where the x -direction loading
14 is compressive. This suggests these cracks may initiate due to the shear loading of the 0° fibre
15 bundles. They then propagate by longitudinal splitting along the bundle interfaces, similarly
16 to delamination from transverse cracking [30]. Similar shear cracking of matrix and
17 interlaminar deflection has been observed in compression testing of a Nextel 610/Alumina
18 composite [28]. The final fracture path is a consequence of the interactions between these
19 propagating shear and delamination cracks with pre-existing defects in the matrix and also at
20 the fibre bundle/matrix interfaces. This proposed sequence of damage development could be
21 confirmed by more frequent tomographs in a future study.

22 The cracking observed at 1100°C was similar to that at room temperature, but needle-like
23 interlayer cracks, aligned parallel to the x -direction of loading, developed additionally
24 between and within the fibre bundles. These cracks were observed in both the tensile and

compressive regions of the flexural specimen, and tended to occur in the regions of highest bending moment, *i.e.*, close to the position of the central loading pin, as well as close to the support pin (**Figures 10, 12**). These are the locations where higher shear strains would be expected between lamellae of different compliance in a laminated composite beam [31].

The elastic properties of the matrix and fibres are essentially constant at the temperatures investigated, so the stresses that develop within the microstructure due to external loading are not expected to differ at room temperature and 1100°C. On cooling from sintering, misfit strains will develop due to differential thermal contraction of the matrix and fibres (alumina ($7.9 \times 10^{-6} \text{ C}^{-1}$) and the Nextel 720 alumino-silicate fibre ($6.0 \times 10^{-6} \text{ C}^{-1}$)) [32]. The fibres have the lower expansion coefficient, so a residual compressive misfit stress would be expected at the fibre-matrix interface [33]. The fibre crystallographic texture may cause anisotropic properties, giving additional stress between the 0° and 90° fibre layers [34–36]. At 1100°C, which is close to the sintering temperature, the thermally induced residual stresses would be significantly relaxed. A reduction in the compressive residual stress between the matrix and fibre would decrease the frictional sliding resistance of the interface, and this may be the cause of the increased tendency for interfacial failure and the needle-like interlayer cracks that is observed at 1100°C at locations of higher shear stress. Interfacial failure could be further encouraged by creep, which has been observed to occur at 1100°C in a Nextel 720/alumina composite at high stress [13].

5. Conclusions

In situ synchrotron x-ray observations of flexural bending tests on a Nextel 720 fibre / alumina matrix CMC, conducted at ambient and 1100°C, show there is a change in failure mechanism at the higher temperature. Measurements of the strain gradient, using digital

1 volume correlation, demonstrate a reduction in effective flexural modulus that is coincident
2 with the observation of mechanical damage as significant internal cracks initiated and
3 propagated close to the flexural strength. At both room temperature and 1100°C, cracks are
4 initiated by the shear of the fibre bundles that are oriented perpendicular to the loading; these
5 cracks are then deflected along the fibre bundle/matrix interfaces. At 1100°C, interlayer
6 cracks also initiated between, and within, the fibre bundles, and caused significant
7 delamination. The change in failure mode at 1100°C may be explained by relaxation of the
8 thermal misfit stresses to decrease the frictional sliding resistance of the fibre/matrix
9 interface, and creep.

Acknowledgements

The research was funded by Cross Manufacturing Ltd, Bath. The UKRI EPSRC Grant EP/M02833X/1 “University of Oxford: experimental equipment upgrade” supported the Xradia Versa 510 microscope and facilities for data analysis and visualization. The authors are grateful to Edward Cross and Paul Blanchard at Cross Manufacturing Ltd, Bath UK, for technical support, and Tim Shumate and Barrett Jackson at Composites Horizons, LLC (PCC Structural, Oregon, United States, for providing technical support., and Composite Horizons, LLC (PCC Structural, USA) for supplying samples. D.L. acknowledges funding from the EPSRC fellowship grant no. EP/N004493/1 and the Royal Commission for the Exhibition of 1851 Research Fellowship grant. The authors acknowledge the use of the x-ray synchrotron microtomography beamline (8.3.2) at the Lawrence Berkeley National Laboratory’s Advanced Light Source, which is supported by the U.S. Department of Energy, Office of Science, Office of Basic Energy Sciences of the U.S. Department of Energy under contract no. DE-AC02-05CH11231. D.L. and R.O.R. would like to thank Dr. Dula Parkinson for help with the synchrotron tomography experiments.

Author Contributions

Talha J. Pirzada: Investigation, writing – original draft; Dong Liu: Conceptualization, investigation; Jon Ell: Investigation; Harold Barnard: Investigation; Ivo Šulák: Investigation; Marina Galano: Supervision, writing - review & editing, Thomas J. Marrow: Conceptualization, supervision, writing – original draft; Robert O. Ritchie: Resources, supervision, writing - review & editing.

Declaration of interests

The authors declare that they have no known competing financial interests or personal relationships that could have appeared to influence the work reported in this paper.

References

- [1] D.B. Marshall, J.B. Davis, Ceramics for future power generation technology: Fiber reinforced oxide composites, *Curr. Opin. Solid State Mater. Sci.* 5 (2001) 283–289.
- [2] F.W. Zok, Developments in oxide fiber composites, *J. Am. Ceram. Soc.* 89 (2006) 3309–3324.
- [3] D. Asmi, I.M. Low, Advances in ceramic matrix composites, in: *Adv. Ceram. Matrix Compos.*, 2nd ed., Woodhead Publishing, Cambridge, 2018: pp. 109–140.
- [4] E. Stoll, P. Mahr, H.G. Krüger, H. Kern, B.J.C. Thomas, A.R. Boccaccini, Fabrication technologies for oxide-oxide ceramic matrix composites based on electrophoretic deposition, *J. Eur. Ceram. Soc.* 26 (2006) 1567–1576.
doi:10.1016/j.jeurceramsoc.2005.03.251.
- [5] V. Mazars, O. Caty, G. Couégnat, A. Bouterf, S. Roux, S. Denneulin, J. Pailhès, G.L. Vignoles, Damage investigation and modeling of 3D woven ceramic matrix composites from X-ray tomography in-situ tensile tests, *Acta Mater.* 140 (2017) 130–139.

- [6] R.A. Jurf, S.C. Butner, Advances in Oxide-Oxide CMC, J. Eng. Gas Turbines Power. 122 (2000) 202–205.
- [7] T.A. Parthasarathy, L.P. Zawada, R. John, M.K. Cinibulk, R.J. Kerans, J. Zelina, Evaluation of oxide-oxide composites in a novel combustor wall application, Int. J. Appl. Ceram. Technol. 2 (2005) 122–132.
- [8] K. Konopka, A. Boczkowska, K. Batorski, M. Szafran, K.J. Kurzydłowski, Microstructure and properties of novel ceramic-polymer composites, Mater. Lett. 58 (2004) 3857–3862.
- [9] M. Ruggles-Wrenn, S. Hilburn, Creep in interlaminar shear of a NextelTM720/aluminosilicate Composite at 1100°C in air and in steam, Int. J. Appl. Ceram. Technol. 12 (2015) 473–480.
- [10] M.K. Cinibulk, Effect of Ytria and Yttrium-Aluminum Garnet on Densification and Grain Growth of Alumina At 1200°--1300° C, J. Am. Ceram. Soc. 87 (2004) 692–695.
- [11] S. Gustafsson, L.K.L. Falk, J.E. Pitchford, W.J. Clegg, E. Lidén, E. Carlström, Development of microstructure during creep of polycrystalline mullite and a nanocomposite mullite/5 vol.% SiC, J. Eur. Ceram. Soc. 29 (2009) 539–550. doi:10.1016/j.jeurceramsoc.2008.06.036.
- [12] S. Hackemann, F. Flucht, W. Braue, Creep investigations of alumina-based all-oxide ceramic matrix composites, Compos. Part A Appl. Sci. Manuf. 41 (2010) 1768–1776.

- [13] C.J. Armani, M.B. Ruggles-Wrenn, R.S. Hay, G.E. Fair, Creep and microstructure of NextelTM 720 fiber at elevated temperature in air and in steam, *Acta Mater.* 61 (2013) 6114–6124. doi:<https://doi.org/10.1016/j.actamat.2013.06.053>.
- [14] R. Bertrand, O. Caty, V. Mazars, S. Denneulin, P. Weisbecker, J. Pailhes, G. Camus, F. Rebillat, In-situ tensile tests under SEM and X-ray computed micro-tomography aimed at studying a self-healing matrix composite submitted to different thermomechanical cycles, *J. Eur. Ceram. Soc.* 37 (2017) 3471–3474.
- [15] L. Saucedo-Mora, T. Lowe, S. Zhao, P.D. Lee, P.M. Mummery, T.J. Marrow, In situ observation of mechanical damage within a SiC-SiC ceramic matrix composite, *J. Nucl. Mater.* 481 (2016) 13–23.
- [16] F. Wan, R. Liu, Y. Wang, Y. Cao, C. Zhang, T.J. Marrow, In situ observation of compression damage in a 3D needled-punched carbon fiber-silicon carbide ceramic matrix composite, *Compos. Struct.* 210 (2019) 189–201. doi:[10.1016/J.COMPSTRUCT.2018.11.041](https://doi.org/10.1016/J.COMPSTRUCT.2018.11.041).
- [17] F. Wan, R. Liu, Y. Wang, Y. Cao, C. Zhang, T.J. Marrow, Damage development during flexural loading of a 5-directional braided C/C-SiC composite, characterized by X-ray tomography and digital volume correlation, *Ceram. Int.* (2018). doi:[10.1016/J.CERAMINT.2018.12.020](https://doi.org/10.1016/J.CERAMINT.2018.12.020).
- [18] A. Haboub, H.A. Bale, J.R. Nasiatka, B.N. Cox, D.B. Marshall, R.O. Ritchie, A.A. Macdowell, Tensile testing of materials at high temperatures above 1700°C with in

situ synchrotron X-ray micro-tomography, *Rev. Sci. Instrum.* 85 (2014).

[19] H.A. Bale, A. Haboub, A.A. MacDowell, J.R. Nasiatka, D.Y. Parkinson, B.N. Cox, D.B. Marshall, R.O. Ritchie, Real-time quantitative imaging of failure events in materials under load at temperatures above 1,600 °C., *Nat. Mater.* 12 (2013) 40–6. doi:10.1038/nmat3497.

[20] D. Liu, B. Gludovatz, H.S. Barnard, M. Kuball, R.O. Ritchie, Damage tolerance of nuclear graphite at elevated temperatures, *Nat. Commun.* 8 (2017). doi:10.1038/ncomms15942.

[21] D. Gürsoy, F. De Carlo, X. Xiao, C. Jacobsen, TomoPy: a framework for the analysis of synchrotron tomographic data, *J. Synchrotron Radiat.* 21 (2014) 1188–1193.

[22] C. Li, G. Habler, L.C. Baldwin, R. Abart, An improved FIB sample preparation technique for site-specific plan-view specimens: A new cutting geometry, *Ultramicroscopy.* 184 (2018) 310–317.

[23] S.R. Eugster, Geometric continuum mechanics and induced beam theories, in: Springer, New York, 2015: pp. 55–81.

[24] G.P. Tandon, D.J. Buchanan, N.J. Pagano, R. John, Analytical and Experimental Characterization of Thermo-Mechanical Properties of a Damaged Woven Oxide-Oxide Composite, in: 25th Annu. Conf. Compos. Adv. Ceram. Mater. Struct. A Ceram. Eng. Sci. Proc., 2001: pp. 687–694.

- [25] M.K. Naskar, M. Chatterjee, A. Dey, K. Basu, Effects of processing parameters on the fabrication of near-net-shape fibre reinforced oxide ceramic matrix composites via sol–gel route, *Ceram. Int.* 30 (2004) 257–265. doi:[https://doi.org/10.1016/S0272-8842\(03\)00097-X](https://doi.org/10.1016/S0272-8842(03)00097-X).
- [26] M. Ruggles-Wrenn, S. Hilburn, Creep in interlaminar shear of a NextelTM720/aluminosilicate Composite at 1100°C in air and in steam, *Int. J. Appl. Ceram. Technol.* 12 (2015) 473–480.
- [27] E. Volkmann, K. Tushtev, D. Koch, C. Wilhelmi, J. Göring, K. Rezwani, Assessment of three oxide/oxide ceramic matrix composites: Mechanical performance and effects of heat treatments, *Compos. Part A Appl. Sci. Manuf.* 68 (2015) 19–28. doi:[10.1016/j.compositesa.2014.09.013](https://doi.org/10.1016/j.compositesa.2014.09.013).
- [28] C. Ben Ramdane, A. Julian-Jankowiak, R. Valle, Y. Renollet, M. Parlier, E. Martin, P. Diss, Microstructure and mechanical behaviour of a NextelTM610/alumina weak matrix composite subjected to tensile and compressive loadings, *J. Eur. Ceram. Soc.* 37 (2017) 2919–2932. doi:[10.1016/j.jeurceramsoc.2017.02.042](https://doi.org/10.1016/j.jeurceramsoc.2017.02.042).
- [29] V. Kostopoulos, T.H. Loutas, A. Kontsos, G. Sotiriadis, Y.Z. Pappas, On the identification of the failure mechanisms in oxide/oxide composites using acoustic emission, *NDT E Int.* 36 (2003) 571–580. doi:[10.1016/S0963-8695\(03\)00068-9](https://doi.org/10.1016/S0963-8695(03)00068-9).
- [30] J.M. Berthelot, J.F. Le Corre, A model for transverse cracking and delamination in cross-ply laminates, *Compos. Sci. Technol.* 60 (2000) 1055–1066.

- [31] S. Cheng, X. Wei, T. Jiang, Stress distribution and deformation of adhesive-bonded laminated composite beams, *J. Eng. Mech.* 115 (1989) 1150–1162.
doi:10.1061/(ASCE)0733-9399(1989)115:6(1150).
- [32] D.M. Wilson, L.R. Visser, High performance oxide fibers for metal and ceramic composites, *Compos. - Part A Appl. Sci. Manuf.* 32 (2001) 1143–1153.
doi:10.1016/S1359-835X(00)00176-7.
- [33] J.B. Davis, R.S. Hay, D.B. Marshall, P.E.D. Morgan, A. Sayir, Influence of interfacial roughness on fiber sliding in oxide composites with La-monazite interphases, *J. Am. Ceram. Soc.* 86 (2003) 305–316. doi:10.1111/j.1151-2916.2003.tb00016.x.
- [34] Y. Nawab, F. Jacquemin, P. Casari, N. Boyard, V. Sobotka, Y. Nawab, F. Jacquemin, P. Casari, N. Boyard, Y. Borjon-piron, Study of variation of thermal expansion coefficients in carbon / epoxy laminated composite plates, *Compos. Part B Eng.* 50 (2013) 144–149.
- [35] T. Ishikawa, K. Koyama, S. Kobayashi, Thermal Expansion Coefficients of Unidirectional Composites, *J. Compos. Mater.* 12 (1978) 153–168.
- [36] W.J. Craft, R.M. Christensen, Coefficient of Thermal Expansion for Composites with Randomly Oriented Fibers, *J. Compos. Mater.* 15 (1981) 2–20.

Figure Captions

Figure 1: Microstructure of as-fabricated oxide-oxide ceramic-matrix composite sample: a) 3D x-ray tomography visualization (2.7 μm voxel); b) Pore segmentation and visualization from x-ray tomograph; c) SEM image of polished section; d) SEM image of fibre/matrix interface.

Figure 2: Scanning transmission electron microscopy (STEM) observations with DF-HAADF dark field (porosity is black) of the matrix/fibre interface of samples tested at (a) room temperature and (b) 1100°C.

Figure 3: Diffraction from fibres (sample RT) obtained at different orientations relative to the fibre axis: (a) azimuthally integrated diffraction spectra (vertical lines show the expected location of the α -alumina peaks, with the $\{113\}$ and $\{223\}$ emphasised); b) diffraction images obtained with beam oriented at i) 0°; ii) 30°; iii) 60° and iv) 90° relative to the fibre axis.

Figure 4: Nominal stress/strain relationships (obtained from load-crosshead displacement) of samples tested using three-point bend test at room temperature (RT) and 1100°C (specimen S2). The vertical lines indicate the regions over which the linear gradients were measured.

Figure 5: Three-point bend test setup showing the regions imaged by tomography (sections are presented at the pre-load) and analysed with digital volume correlation (DVC), in relation to the loading and support pins at a) room temperature and b) 1100°C. (S1 and S2 are the volumes tomographed at different resolution: a tomograph section from S1 is shown). The theoretical shear force (F_s) and bending moment (M) diagram is also shown, as a function of load, P .

Figure 6: Cross-sectional examination of tested specimens: Nomarski optical microscopy images of samples tested at (a) room temperature and (b) 1100°C. The dotted box in (a) and (b) shows the area analysed by scanning electron microscopy for samples tested at (c) room temperature and (d) 1100°C. The side labelled 'L' indicated the compressive surface on which the loading pin was located.

Figure 7: Central orthoslices (x-y plane) of tomographs at room temperature (3.25 μm voxel); a) with increasing load from the pre-load to $R\sigma$; b) magnified images at selected regions (i) to (iii) with increasing load. The locations of the load and support pins, and the 0° (parallel to x-axis) and 90° (parallel to z-axis) fibre bundles, are indicated.

Figure 8: 3D visualizations from different perspectives (a, b) of the significant cracks developed at $R\sigma$ in the room temperature test, observed by x-ray tomography. The locations of the loading and support pins are indicated in (a). The newly developed cracks (ii) and (iii) are shown in blue, with the pre-existing defects in red.

Figure 9: Central orthoslices (x-y plane) of tomographs at 1100°C (sample S1, 3.25 μm voxel); a) with increasing load from the pre-load to $R\sigma$; b) magnified images at selected regions (i) to (iii) with increasing load. The locations of the load and support pins, and the 0° (parallel to x-axis) and 90° (parallel to z-axis) fibre bundles, are indicated.

Figure 10: Visualizations (a, b) of the significant cracks developed at $R\sigma$ at 1100°C in sample S1, observed by *in situ* x-ray tomography. The locations of the loading pin can be seen in (a). The newly developed cracks of two different types are identified: (i) through the cross section (blue) and (ii) needle shaped (purple).

Figure 11: Central orthoslices (x-y plane) of tomographs at 1100°C (sample S2, 1.3 μm voxel); a) with increasing load from the pre-load to $R\sigma$; b) magnified images at selected regions (i) to (iii) with increasing load. The locations of the load and support pins, and the 0° (parallel to x-axis) and 90° (parallel to z-axis) fibre bundles, are indicated.

Figure 12: Visualizations from different perspectives (a, b) of the significant cracks developed at $R\sigma$ at 1100°C (sample S2), observed by *in situ* x-ray tomography. The location of the loading pin is indicated. An orthoslice (x-y plane) of the tomograph at $R\sigma$ is shown in c). The cracks labelled (i) are examples of pre-existing cracks in the matrix, whereas those labelled (ii) initiated prior to failure.

Figure 13: Central orthoslices (x-y plane) of the maximum normal 3D strain field measured by DVC of *in situ* x-ray tomographs at room temperature (referenced to the pre-load): a) with increasing load from the 0.5 $R\sigma$ to $R\sigma$; b) magnified images at selected regions (i) to (iii) with increasing load. The locations of the load and support pins, and the 0° and 90° fibre bundles, are indicated. The backgrounds are orthoslices of the loaded tomograph at the same location. All images have the same strain scale.

Figure 14: Analysis of the relative displacements, calculated at $R\sigma$ relative to the pre-load, across a major crack developed at room temperature, identified in **Figure 13b**; (ii): a) sections of the 3D displacement field, showing the components of the x- and y-displacement; b) the relative opening and shear displacements measured parallel and perpendicular to traces A to F, which are labelled in (a). The error bars are the sample standard deviation from measurements over a z-distance of 75 μm .

Figure 15: Central orthoslices (x-y plane) of the maximum normal 3D strain field measured by DVC of *in situ* x-ray tomographs of sample S2 at 1100°C (referenced to the pre-load):

a) at $R\sigma$; b) magnified images at selected regions (i) to (iii) at $R\sigma$. The locations of the load and support pins, and the 0° and 90° fibre bundles, are indicated. The backgrounds are orthoslices of the loaded tomograph at the same location. All images have the same strain scale.

Figure 16: Analysis of the relative displacements, calculated at $R\sigma$ relative to the pre-loaded state, across a crack developed at 1100°C (sample S2): a) sections of the 3D displacement field, showing the components of the x- and y-displacement; b) the relative opening and shear displacements measured parallel and perpendicular to traces A to F, which are labelled in (a). The error bars are the sample standard deviation from measurements over a z-distance of $75\text{ }\mu\text{m}$.

Figure 17: Flexural strain gradient measurement: (a) Schematic of the y-z planes, separated by a distance of 0.70 mm , between which the relative x-displacements were measured to obtain the average flexural strains, ε_x , at the location of maximum bending moment; (b) maps of the flexural strain, ε_x , with increasing load up to $R\sigma$ at room temperature; (c) the normalized flexural strain, $(\varepsilon_x I/M)$ as a function of distance in the y direction from the beam centre for different loads at room temperature (RT) and at 1100°C (samples S1 and S2). The data are averaged in z, I is the second moment of area of beam cross-section, and M is the change in applied bending moment. The error bars are the standard deviation of the measurements.

1 **Table Captions**

2 **Table 1:** Areas (and mean ratio) of the alumina {113} and {223} diffraction peaks with beam
3 angle relative to the fibre axis.

4 **Table 2:** Mechanical properties obtained from three-point bend tests at room temperature
5 (RT) and 1100°C (**Figure 4**). Duplicate tests that were not observed by tomography are
6 shown in brackets. The uncertainties are the measurement error, and for the effective flexural
7 modulus the variance of the best linear fit gradient.

8 **Table 3:** The effective flexural modulus (GPa) obtained by linear fit to the normalised
9 flexural strains (**Figure 17c**) for different loads at room temperature (RT) and 1100°C. The
10 uncertainty is from the variance of the best fit gradient.

11

Tables

Table 1: Areas (and mean ratio) of the alumina {113} and {223} diffraction peaks with beam angle relative to the fibre axis.

Rotation Angle (°)	{113}	{223}	Ratio
0	5.68±0.05	1.31±0.05	4.3
30	7.89±0.05	1.14±0.05	6.9
60	5.71±0.05	2.81±0.05	2.0
90	5.90±0.05	3.49±0.05	1.7

Table 2: Mechanical properties obtained from three-point bend tests at room temperature (RT) and 1100°C (**Figure 4**). Duplicate tests, not observed by tomography, are shown in brackets. The uncertainties are the measurement error, and for the effective flexural modulus the variance of the best linear fit gradient.

Test Temperature	RT	1100°C
Flexural stress at fracture (MPa)	107±0.4 (103±0.7)	100±0.6 (98±0.8)
Effective Flexural modulus (GPa)	51.6±0.8	42.5±0.7

1

2 **Table 3:** The effective flexural modulus (GPa) obtained by linear fit to the normalised flexural strains
 3 (Figure 17c) for different loads at room temperature (RT) and 1100°C. The uncertainty is from the
 4 variance of the best fit gradient.

Stress (Rσ)	RT	1100°C (S1)	1100°C (S2)
0.5	37.9±1.4		
0.8	34.7±1.9		40.1±2.4
1.0	33.2±3.2	26.6±3.7	35.9±4.1

5

Figures

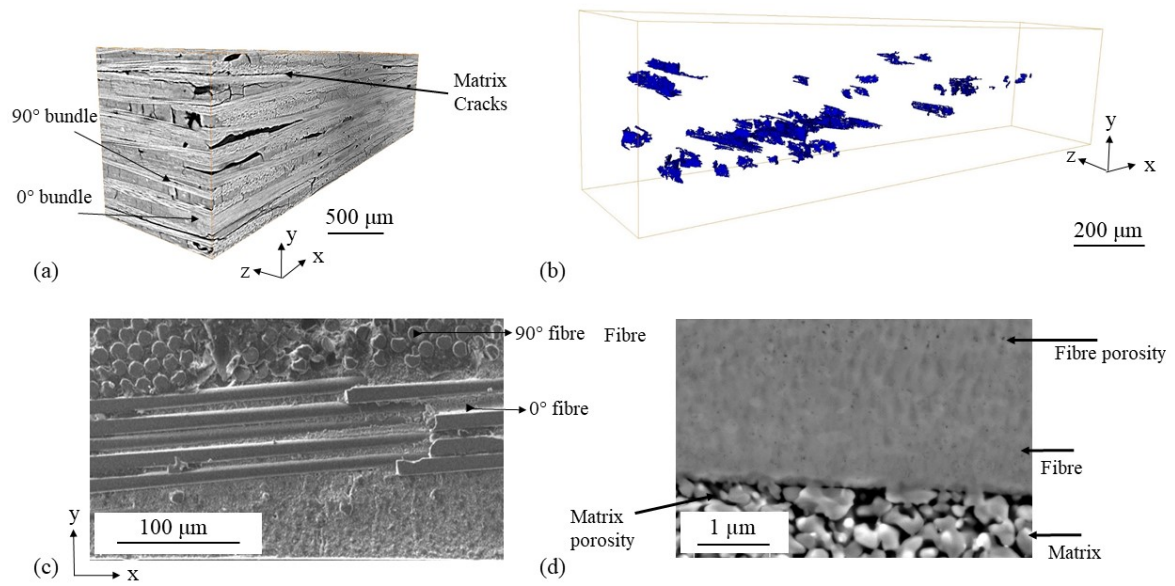


Figure 1: Microstructure of as-fabricated oxide-oxide ceramic-matrix composite sample: a) 3D x-ray tomography visualization (2.7 μm voxel); b) Pore segmentation and visualization from x-ray tomograph; c) SEM image of polished section; d) SEM image of fibre/matrix interface.

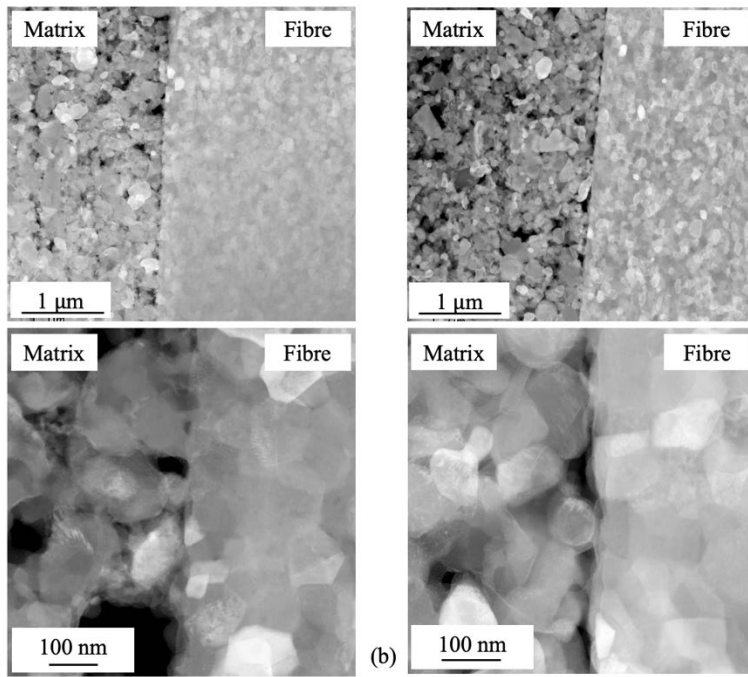


Figure 2: Scanning transmission electron microscopy (STEM) observations with DF-HAADF dark field (porosity is black) of the matrix/fibre interface of samples tested at (a) room temperature and (b) 1100°C.

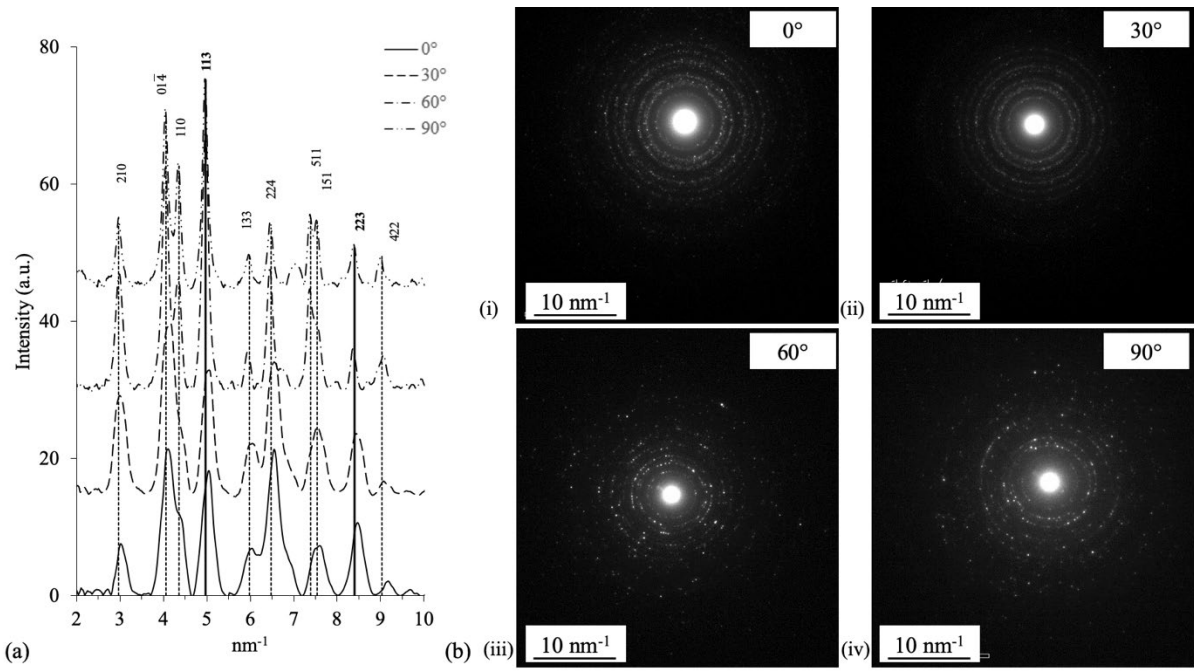
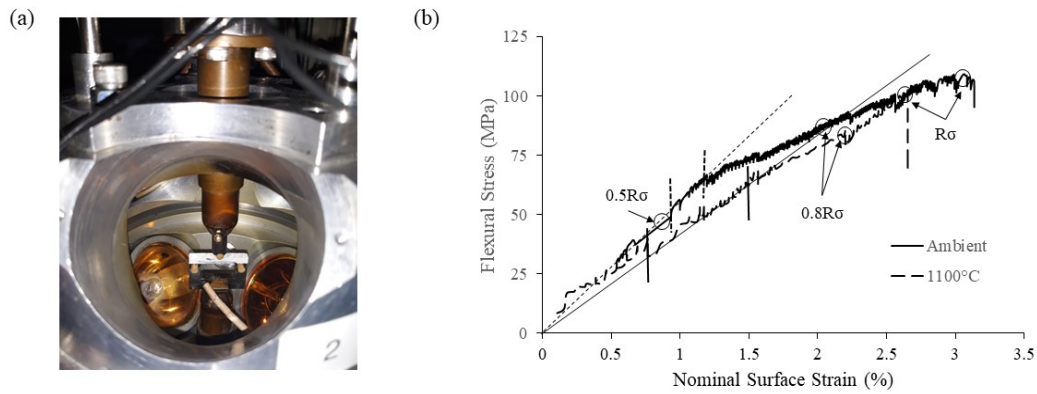


Figure 3: Diffraction from fibres (sample RT) obtained at different orientations relative to the fibre axis: (a) azimuthally integrated diffraction spectra (vertical lines show the expected location of the α -alumina peaks, with the $\{113\}$ and $\{223\}$ emphasised); b) diffraction images obtained with beam oriented at i) 0° ; ii) 30° ; iii) 60° and iv) 90° relative to the fibre axis.

1



2

3 **Figure 4:** (a) The setup used to carry out the three point bend test (b) Stress strain curve of samples
 4 tested using three point bend test at room temperature and elevated temperature, S2. The straight
 5 lines at around 45° angle were used to calculate the modulus of the curve. The vertical lines indicated
 6 the region from which the gradient was measured

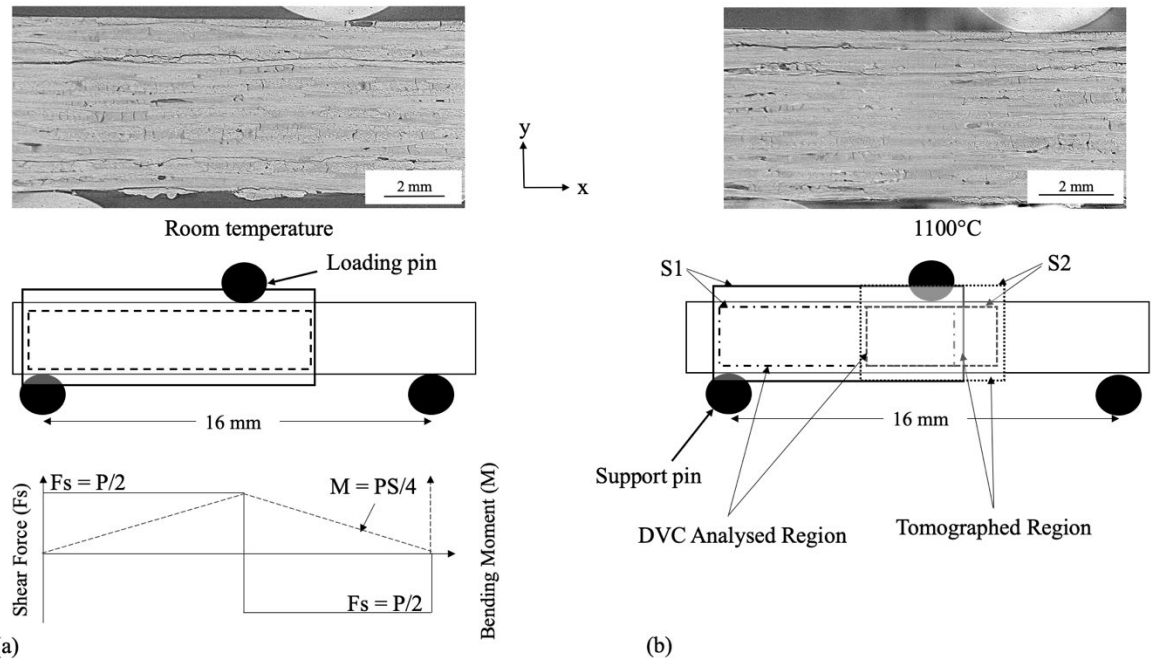


Figure 5: Three-point bend test setup showing the regions imaged by tomography (sections are presented at the pre-load) and analysed with digital volume correlation (DVC), in relation to the loading and support pins at a) room temperature and b) 1100°C. (S1 and S2 are the volumes tomographed at different resolutions: a tomograph section from S1 is shown). The theoretical shear force (F_s) and bending moment (M) diagram is also shown, as a function of load, P .

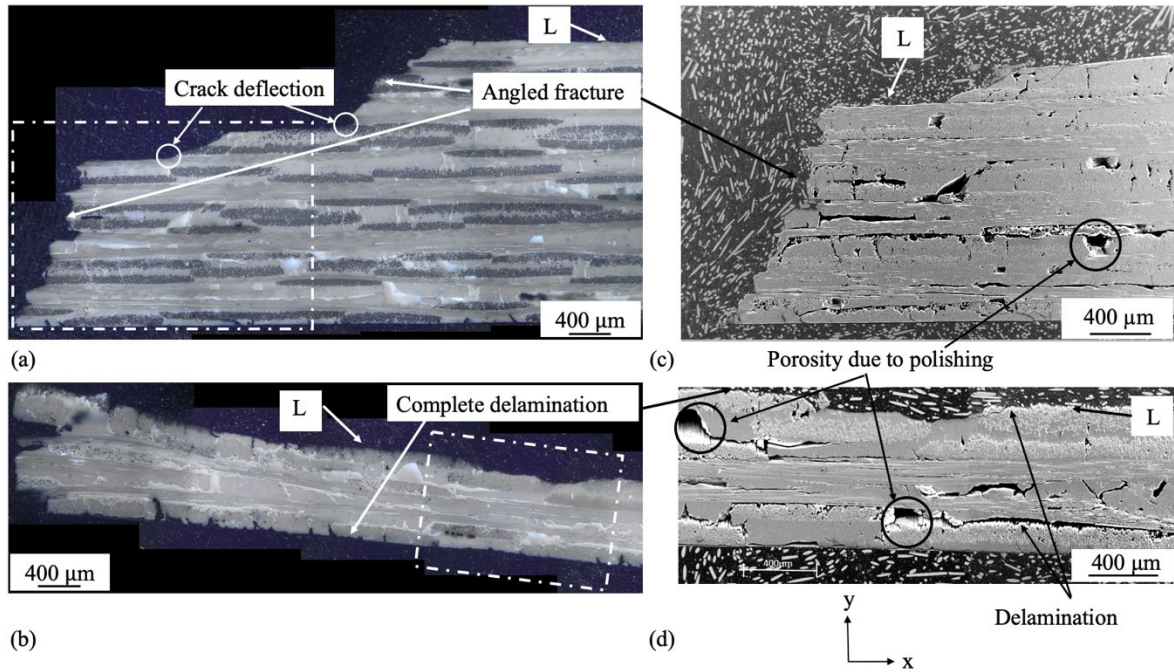


Figure 6: Cross-sectional examination of tested specimens: Nomarski optical microscopy images of samples tested at (a) room temperature and (b) 1100°C. The dotted box in (a) and (b) shows the area analysed by scanning electron microscopy for samples tested at (c) room temperature and (d) 1100°C. The side labelled 'L' indicated the compressive surface on which the loading pin was located.

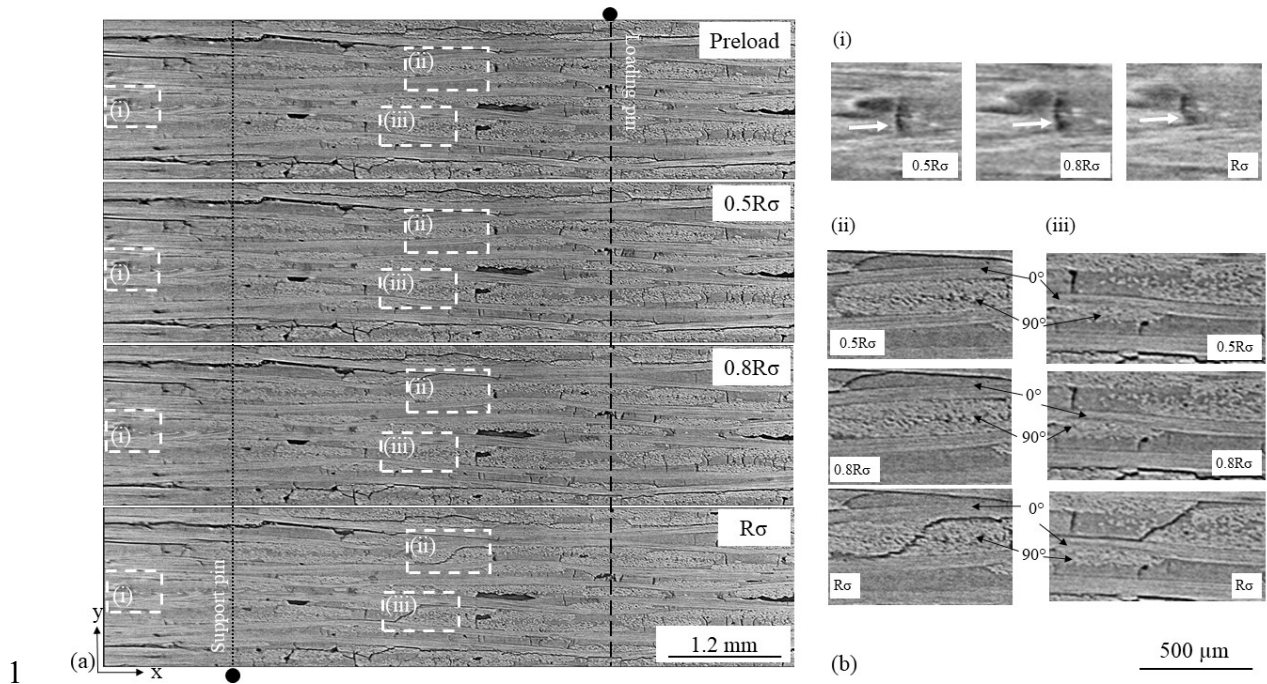


Figure 7: Central orthoslices (x-y plane) of tomographs at room temperature ($3.25\ \mu\text{m}$ voxel); a) with increasing load from the pre-load to $R\sigma$; b) magnified images at selected regions (i) to (iii) with increasing load. The locations of the load and support pins, and the 0° (parallel to x-axis) and 90° (parallel to z-axis) fibre bundles, are indicated.

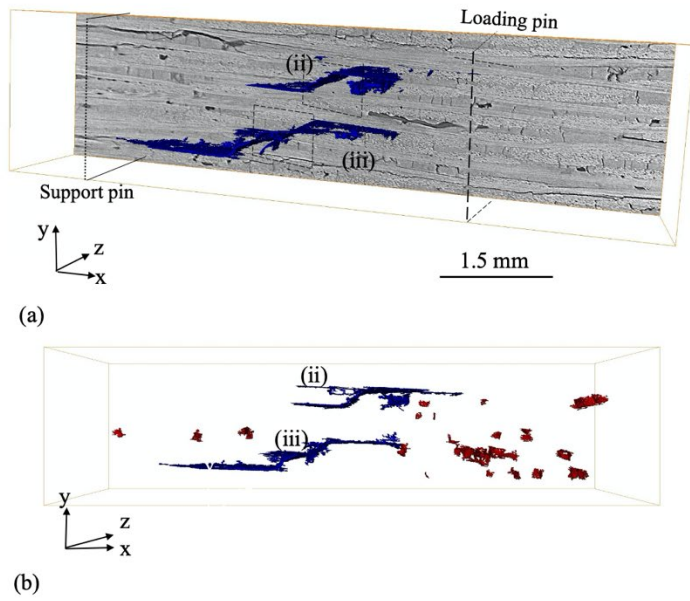
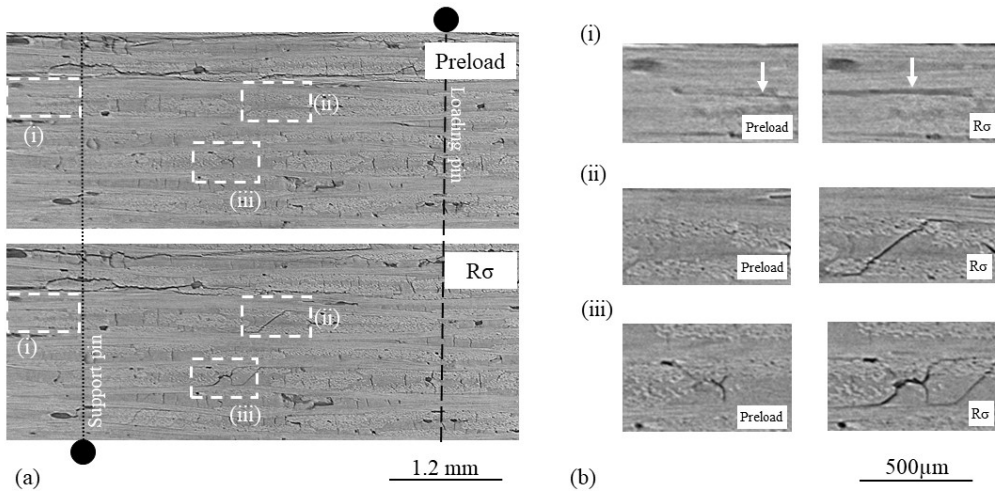


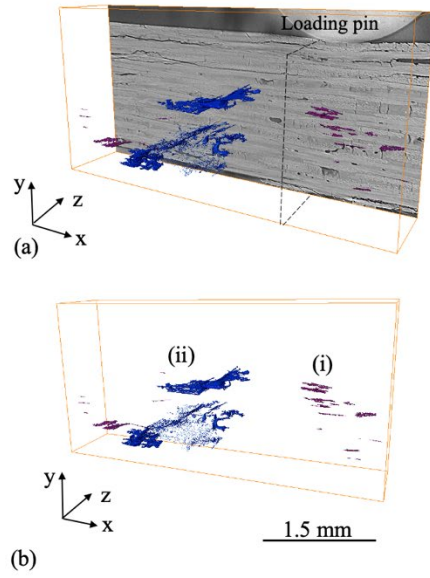
Figure 8: 3D visualizations from different perspectives (a, b) of the significant cracks developed at $R\sigma$ in the room temperature test, observed by x-ray tomography. The locations of the loading and support pins are indicated in (a). The newly developed cracks (ii) and (iii) are shown in blue, with the pre-existing defects in red.

1



2

3 **Figure 9:** Central orthoslices (x-y plane) of tomographs at 1100°C (sample S1, 3,25 μm voxel); a)
 4 with increasing load from the pre-load to $R\sigma$; b) magnified images at selected regions (i) to (iii) with
 5 increasing load. The locations of the load and support pins, and the 0° (parallel to x-axis) and 90°
 6 (parallel to z-axis) fibre bundles, are indicated.



1

2

3

4

5

Figure 10: Visualizations (a , b) of the significant cracks developed at $R\sigma$ at 1100°C in sample S1, observed by in situ x-ray tomography. The locations of the loading pin can be seen in (a). The newly developed cracks of two different types are identified: (i) through the cross section (blue) and (ii) needle shaped (purple).

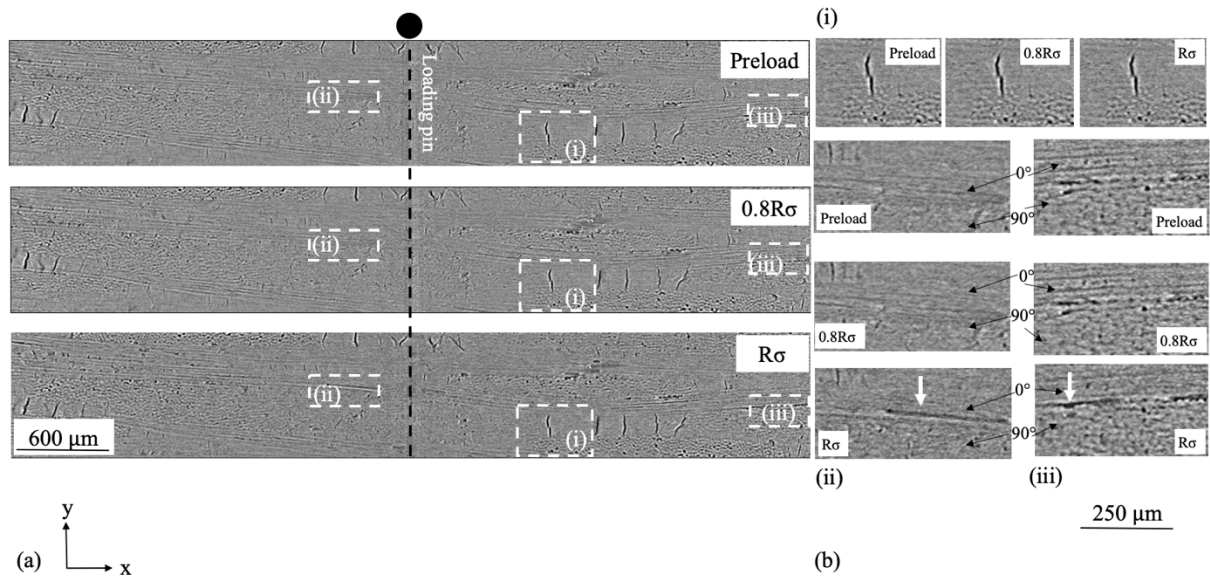


Figure 11: Central orthoslices (x - y plane) of tomographs at 1100°C (sample S2, 1.3 μm voxel); a) with increasing load from the pre-load to $R\sigma$; b) magnified images at selected regions (i) to (iii) with increasing load. The locations of the load and support pins, and the 0° (parallel to x -axis) and 90° (parallel to z -axis) fibre bundles, are indicated.

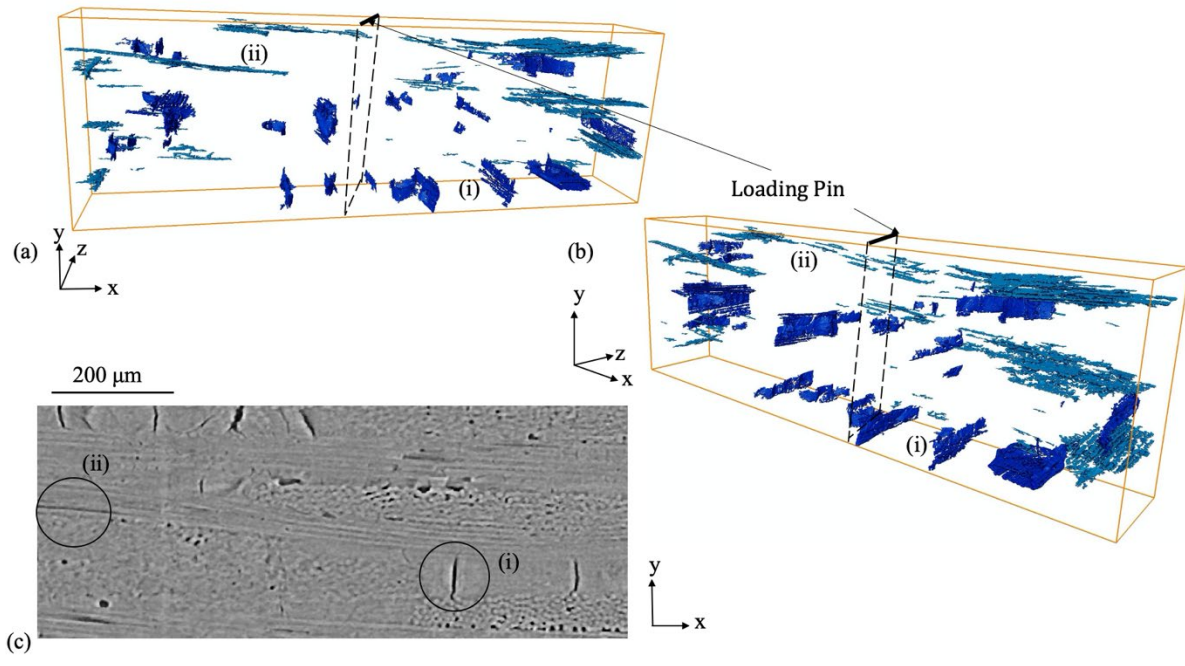


Figure 12: Visualizations from different perspectives (a , b) of the significant cracks developed at $R\sigma$ at 1100°C (sample S2), observed by in situ x-ray tomography. The location of the loading pin is indicated. An orthoslice (x-y plane) of the tomograph at $R\sigma$ is shown in c). The cracks labelled (i) are examples of pre-existing cracks in the matrix, whereas those labelled (ii) initiated prior to failure.

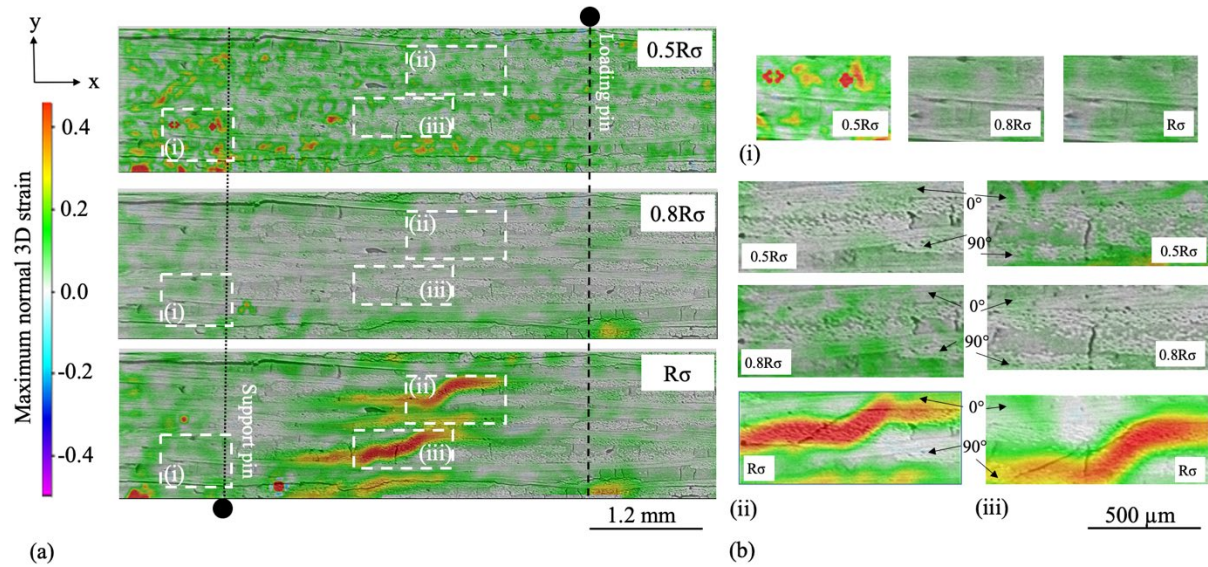


Figure 13: Central orthoslices (x - y plane) of the maximum normal 3D strain field measured by DVC of in situ x-ray tomographs at room temperature (referenced to the pre-load): a) with increasing load from the $0.5R\sigma$ to $R\sigma$; b) magnified images at selected regions (i) to (iii) with increasing load. The locations of the load and support pins, and the 0° and 90° fibre bundles, are indicated. The backgrounds are orthoslices of the loaded tomograph at the same location. All images have the same strain scale.

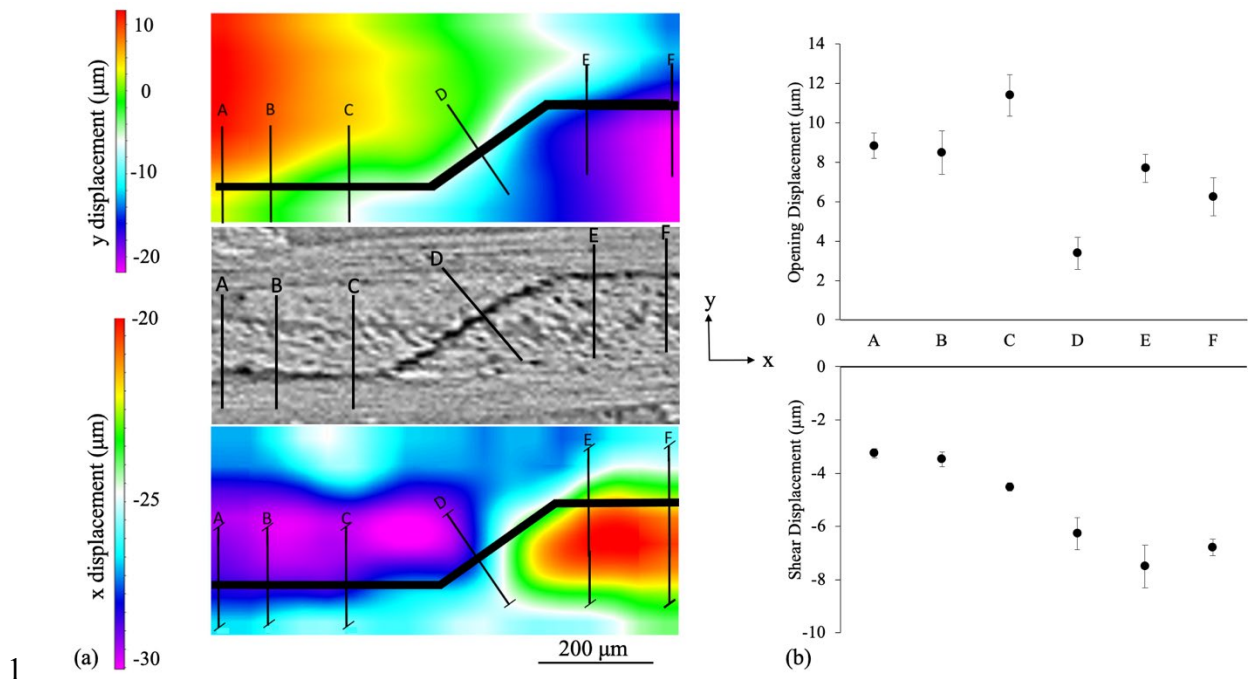


Figure 14: Analysis of the relative displacements, calculated at $R\sigma$ relative to the pre-load, across a major crack developed at room temperature, identified in **Figure 13b**; (ii): a) sections of the 3D displacement field, showing the components of x- and y-displacement; b) the relative opening and shear displacements measured parallel and perpendicular to traces A to F, which are labelled in (a). The error bars are the sample standard deviation from measurements over a z-distance of 75 μm.

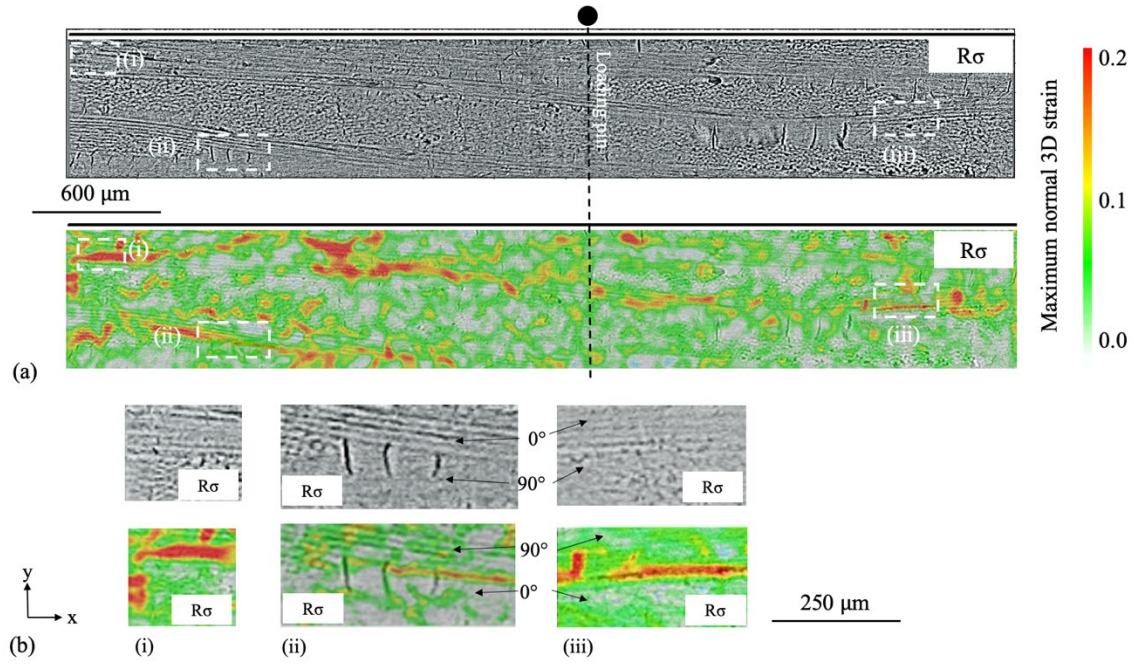


Figure 15: Central orthoslices (x-y plane) of the maximum normal 3D strain field measured by DVC of in situ x-ray tomographs of sample S2 at 1100°C (referenced to the pre-load): a) at $R\sigma$; b) magnified images at selected regions (i) to (iii) at $R\sigma$. The locations of the load and support pins, and the 0° and 90° fibre bundles, are indicated. The backgrounds are orthoslices of the loaded tomograph at the same location. All images have the same strain scale.

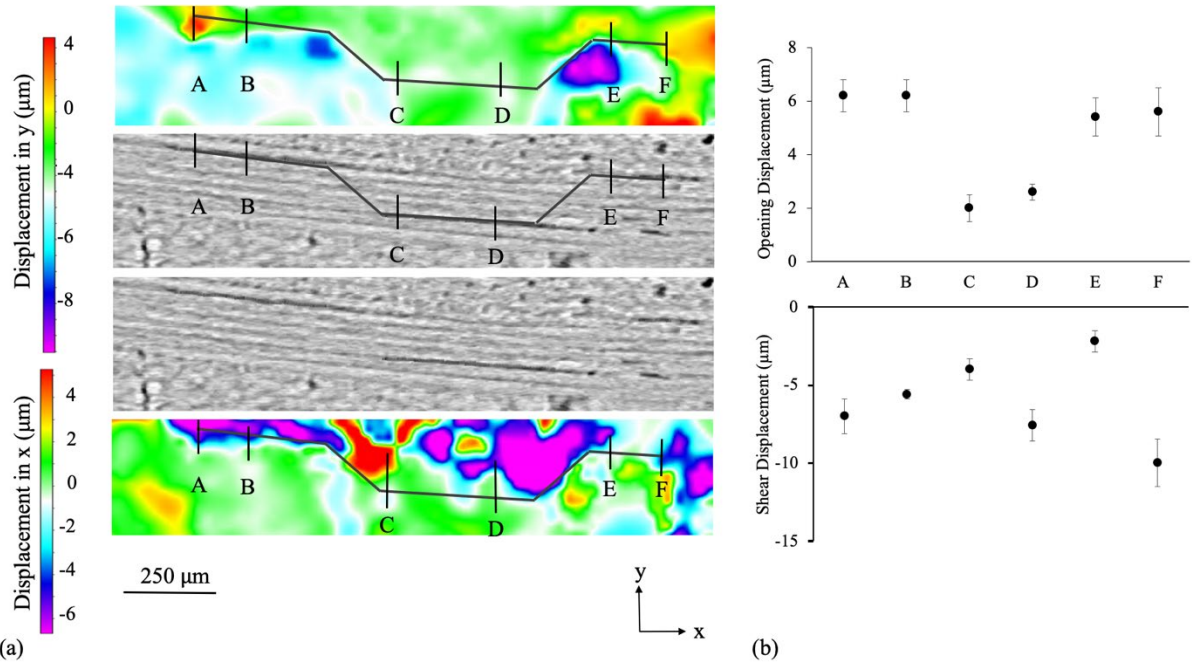


Figure 16: Analysis of the relative displacements, calculated at $R\sigma$ relative to the pre-loaded state, across a crack developed at 1100°C (sample S2): a) sections of the 3D displacement field, showing the components of x- and y-displacement; b) the relative opening and shear displacements measured parallel and perpendicular to traces A to F, which are labelled in (a). The error bars are the sample standard deviation from measurements over a z-distance of 75 μm. .

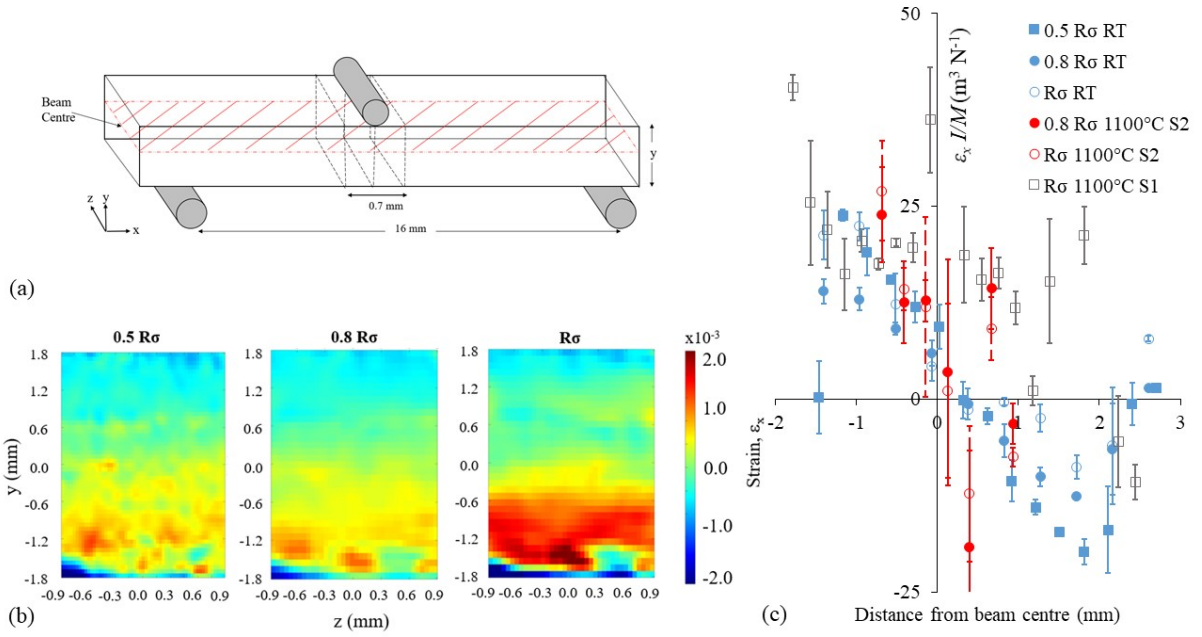


Figure 17: Flexural strain gradient measurement: (a) Schematic of the y-z planes, separated by a distance of 0.70 mm, between which the relative x-displacements were measured to obtain the average flexural strains, ϵ_x , at the location of maximum bending moment; (b) maps of the flexural strain, ϵ_x , with increasing load up to $R\sigma$ at room temperature; (c) the normalized flexural strain, $(\epsilon_x I / M)$ as a function of distance in the y direction from the beam centre for different loads at room temperature (RT) and at 1100°C (samples S1 and S2). The data are averaged in z, I is the second moment of area of beam cross-section, and M is the change in applied bending moment. The error bars are the standard deviation of the measurements.